Strain gradient plasticity in gradient structured metals

Yin Zhang[a], Zhao Cheng[b], Lei Lu[b], Ting Zhu[a],*

[a] Woodruff School of Mechanical Engineering, Georgia Institute of Technology, Atlanta, GA, 30332, USA
[b] Shenyang National Laboratory for Materials Science, Institute of Metal Research, Chinese Academy of Sciences, Shenyang, 110016, China

ARTICLE INFO

ABSTRACT

Structural gradients in metallic materials can give rise to substantial extra strengths compared to their non-gradient counterparts. This strengthening effect originates from the plastic strain gradients arising in plastically deformed gradient structures. Here we develop a gradient theory of plasticity by incorporating the strengthening effect of plastic strain gradients into the classical J_2 flow theory. This gradient theory is numerically implemented to study the strain gradient plasticity in gradient nanotwinned (GNT) Cu with different twin thickness gradients and accordingly different built-in strength gradients. Numerical simulations reveal the primary features of gradient plasticity in GNT Cu under uniaxial tension, including progressive yielding, gradient distributions of plastic strain and extra plastic flow resistance. The combined simulation and experimental results show that the extra strength of GNT Cu depends on the square root of the built-in strength gradient and also on the square root of the saturated plastic strain gradient in fully yielded GNT samples. This finding enables the predictions of optimal gradient structures and associated gradient strength distributions, which suggest possible routes for achieving the maximum strength of GNT Cu.

© 2020 Elsevier Ltd. All rights reserved.

1. Introduction

Gradient structured metals have received considerable attention in recent years due to their enhanced strength, ductility and fatigue resistance compared to non-gradient counterparts (Lu, 2016; Ma and Zhu, 2017; Wu and Zhu, 2017). Structural gradients lead to plastic strain gradients (Aifantis, 1984; Ashby, 1970; Bassani, 2001; Fleck et al., 1994; Gudmundson, 2004; Lele and Anand, 2008, 2009; Niordson and Hutchinson, 2003; Nix and Gao, 1998) that can give rise to substantial extra strengths (Cheng et al., 2018; Fang et al., 2011; Wu et al., 2014). However, the mechanics of gradient plasticity in gradient structures has not been clearly understood (Li and Soh, 2012; Li et al., 2017; Wei et al., 2014; Zeng et al., 2016).

Recently, Cheng et al. (Cheng et al., 2018) reported the fabrication of gradient nanotwinned (GNT) Cu having different gradient distributions of nanoscale twin thicknesses and thus different built-in yield strength gradients. They showed that an increase in the nanostructural gradient, along with a concomitant increase in the strength gradient, causes a marked increase of the sample-level yield strength; and a large nanostructural gradient produces a high sample-level yield strength exceeding that of the strongest component in the gradient nanostructure. In particular, they measured the sample-level extra strength that increases with the built-in strength gradient in a nonlinear manner. These results call for a fundamental understanding of the strengthening effects of plastic strain gradients arising from gradient nanostructures. In addition, given

---

* Corresponding author.
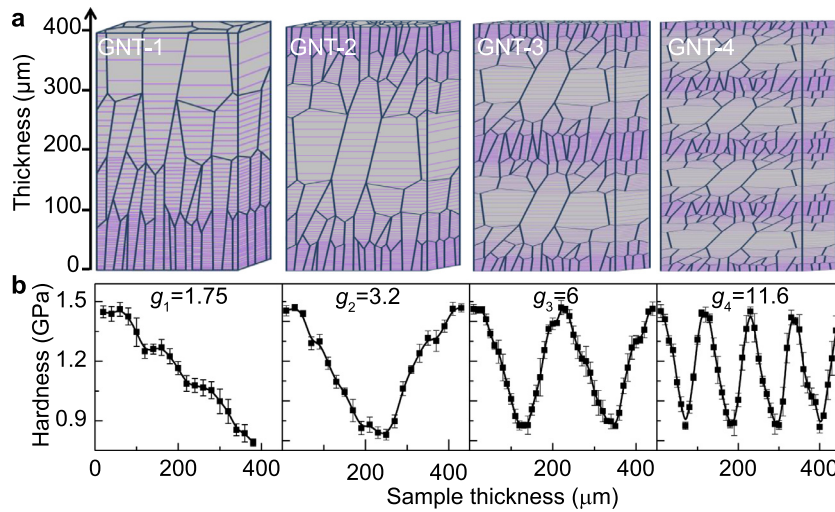*E-mail address:* ting.zhu@me.gatech.edu (T. Zhu).

Fig. 1. Four types of GNT Cu samples, named GNT-1, GNT-2, GNT-3 and GNT-4, respectively (Cheng et al., 2018). (a) Schematic illustration of GNT-1 to GNT-4 samples. Through sample thickness, gradient twin structures exhibit periodic, piecewise linear, continuous variations of twin thickness, in conjunction with gradient grain sizes. Preferentially oriented nanometer-scale twin lamellas (with twin boundaries represented by purple lines) are embedded within micrometer-scale columnar-shaped grains (with grain boundaries represented by blue lines). (b) Measured micro-indentation hardness profiles through the sample thickness of GNT-1 to GNT-4. Each hardness curve is labeled with its corresponding hardness gradient *g* (in unit of GPa/mm). (For interpretation of the references to colour in this figure legend, the reader is referred to the web version of this article.)

the high tunability of its gradient structures, GNT Cu can serve as an effective model system for benchmarking the gradient theories of plasticity.

In this paper, we develop a gradient theory of plasticity by incorporating the strengthening effect of plastic strain gradients into the J_2 flow theory. Motivated by the lower-order gradient theory of plasticity by Bassani (Bassani, 2001), we introduce a scalar measure of plastic strain gradients into a hardening rate relation, so that higher order stresses and additional boundary conditions are not needed. This approach enables an effective analysis of strain gradient plasticity without much mathematical complexity. To study the gradient plastic responses of GNT Cu under uniaxial tension, we reduce the general three-dimensional (3D) gradient theory into a one-dimensional (1D) theory, and numerically implement this 1D theory with the finite difference method. The associated numerical results reveal the primary effects of strain gradient plasticity on GNT Cu with different structural gradients. In addition, we numerically implement the 3D gradient theory into the general finite element package ABAQUS/Explicit (ABAQUS/Explicit, 2016). Numerical results from 3D gradient plasticity finite element (GPFE) simulations confirm those from 1D finite difference simulations, and further reveal the impact of stress components neglected in the 1D gradient theory and simulations. Based on insights gained from these gradient plasticity simulations, we explore the optimization of strength gradients toward achieving the maximum strength of GNT Cu.

2. Experiment

Here we provide a brief overview of the experimentally measured structural and strength gradients in GNT Cu. These results provide a basis for our development of the gradient plasticity theories and associated computational models. As described in detail by Cheng et al. (Cheng et al., 2018), direct current electrodeposition was used to prepare GNT Cu samples with a controlled pattern of gradient nanotwinned structures. Fig. 1a shows the schematic illustration of four types of GNT Cu samples, named GNT-1, GNT-2, GNT-3 and GNT-4, respectively. The corresponding electron microscopy images of GNT microstructures can be found in Cheng et al. (Cheng et al., 2018). These samples have a similar thickness *L* around 400 μm, but different structural gradients through sample thickness. At each local region, preferentially oriented nanometer-scale twin lamellas are embedded within micrometer-scale columnar-shaped grains. As schematically illustrated in Fig. 1a, GNT-1 exhibits approximately linear variations of twin thickness and grain size through sample thickness; the average twin thickness increases from 29 nm to 72 nm, with a concomitant increase of the average grain size from 2.5 μm to 15.8 μm. Despite the dual gradient variations of twin thickness and grain size, the strengthening effects are mainly controlled by the gradient distributions of twin lamellas (Cheng et al., 2018), due to their much smaller twin thicknesses than grain sizes. Hereafter, our description of structural gradients will focus on gradient distributions of nanotwinned structures. As also illustrated in Fig. 1a, GNT-2, GNT-3 and GNT-4 exhibit periodic, piecewise linear, continuous variations of twin thickness (Cheng et al., 2018), which can be approximately represented by triangle waves of twin thickness with different wavelengths, i.e., about *L*, *L*/2 and *L*/3.5, respectively. In fact, the linear profile of twin thickness in GNT-1 can be represented by the half period of a triangle wave with wavelength 2*L*. For GNT-2 to GNT-4, the maximum and minimum twin thicknesses are close to those of GNT-1. As such, their twin thickness gradients are 2, 4 and 7 times that of GNT-1. We note that the control of

structural gradients becomes increasingly difficult with decreasing twin thickness. As a result, GNT-4 has an actual sample thickness larger than 400 μm, such that its twin thickness gradient is not as ideal as 8 times that of GNT-1.

Gradient nanotwinned structures lead to gradient strengths in GNT Cu. Fig. 1b shows the measured micro-indentation hardness profiles of GNT-1 to GNT-4 through sample thickness, which can also be represented by triangle waves of hardness with different wavelengths, i.e., about $2L$, L, $L/2$ and $L/3.5$, respectively. These triangle wave profiles have the approximately identical maximum hardness 1.5 GPa and minimum hardness 0.8 GPa. The measured hardness gradient, denoted as g, for GNT-1 to GNT-4 is 1.75, 3.2, 6.0 and 11.6 GPa/mm, respectively. An increase in hardness gradient causes a marked increase in the sample-level yield strength (Cheng et al., 2018). This result will be presented along with the experimentally measured stress-strain curves of GNT Cu in Section 4, where it will be compared with the corresponding gradient plasticity simulation result.

3. A theory of strain gradient plasticity

To study the mechanical behavior of GNT Cu, we develop a lower-order theory of strain gradient plasticity by incorporating the strengthening effect of plastic strain gradients into the classical J_2 flow theory. In the following, we present the gradient theory using index notation – a free index ranges over 1 to 3 and repeated indices mean summation. The total strain rate $\dot{\varepsilon}_{ij}$ is decomposed into

$$\dot{\varepsilon}_{ij} = \dot{\varepsilon}_{ij}^{e} + \dot{\varepsilon}_{ij}^{p} \tag{1}$$

In Eq. (1), the elastic strain rate $\dot{\varepsilon}_{ij}^{e}$ is related to the stress rate $\dot{\sigma}_{ij}$ by the generalized Hooke's law

$$\dot{\varepsilon}_{ij}^{e} = \frac{1}{E}\left[(1+\nu)\dot{\sigma}_{ij} - \nu\dot{\sigma}_{kk}\delta_{ij}\right] \tag{2}$$

where E is Young's modulus, ν is Poisson's ratio, $\delta_{ij} = 1$ when $i = j$ and $\delta_{ij} = 0$ otherwise. The plastic strain rate $\dot{\varepsilon}_{ij}^{p}$ obeys the J_2 flow rule

$$\dot{\varepsilon}_{ij}^{p} = \dot{\bar{\varepsilon}}^{p}\frac{3\sigma_{ij}'}{2\overline{\sigma}} \tag{3}$$

In Eq. (3), σ_{ij}' is the deviatoric stress given by $\sigma_{ij}' = \sigma_{ij} - \sigma_{kk}\delta_{ij}/3$, $\bar{\sigma}$ is the equivalent stress

$$\overline{\sigma} = \sqrt{\frac{3}{2}\sigma_{ij}'\sigma_{ij}'} \tag{4}$$

and $\dot{\bar{\varepsilon}}^{p}$ is the equivalent plastic strain rate given by a simple power-law relation

$$\dot{\bar{\varepsilon}}^{p} = \dot{\bar{\varepsilon}}_0^{p}\left(\frac{\overline{\sigma}}{s}\right)^{1/m} \tag{5}$$

where $\dot{\bar{\varepsilon}}_0^{p}$ is the reference plastic strain rate, s is the plastic flow resistance that evolves with plastic deformation, and m is the strain rate sensitivity parameter. The accumulated equivalent plastic strain is given by $\overline{\varepsilon}^p = \int_0^t \dot{\bar{\varepsilon}}^p dt'$.

In the current gradient plasticity theory, the initial value of the plastic flow resistance s (equivalent to initial yield strength) is prescribed as a function of spatial coordinate for a given GNT model. Under applied load, s increases with both plastic strain and plastic strain gradient in a nonlinear manner. Specifically, an effective measure of plastic strain gradients is introduced into a hardening rate relation, as motivated by the gradient theory of plasticity from Bassani (Bassani, 2001). That is, the instantaneous hardening rate is given by

$$\dot{s} = h\dot{\bar{\varepsilon}}^p \tag{6}$$

where the hardening rate coefficient h is

$$h = \frac{h_0}{1 + \left(\overline{\varepsilon}^p/\varepsilon_1\right)^{n_1}}\left[1 + \frac{\kappa\sqrt{\alpha}}{1 + \left(\overline{\varepsilon}^p/\varepsilon_2\right)^{n_2}}\right] \tag{7}$$

In Eq. (7), the term outside the square bracket represents the conventional hardening effect of plastic strain. In this term, h_0 is the hardening rate constant; ε_1 and n_1 control the nonlinear behavior of plastic strain hardening, such that the rate of plastic strain hardening when $\overline{\varepsilon}^p > \varepsilon_1$ becomes much smaller than that when $\overline{\varepsilon}^p < \varepsilon_1$. Note that in Eq. (7), the second term inside the square bracket reflects the extra hardening effect due to plastic strain gradients. Here α is defined as

$$\alpha = \sqrt{\overline{\varepsilon}^p_{,i}\overline{\varepsilon}^p_{,i}} \tag{8}$$

which is a scalar measure of spatial gradients of the accumulated equivalent plastic strain $\overline{\varepsilon}^p_{,i} = \partial\overline{\varepsilon}^p/\partial x_i$. As such, the hardening rate due to plastic strain gradients scales with $\kappa\sqrt{\alpha}h_0$, where κ is a constant with the unit of $\sqrt{\mathrm{m}}$, and $\kappa\sqrt{\alpha}$ serves
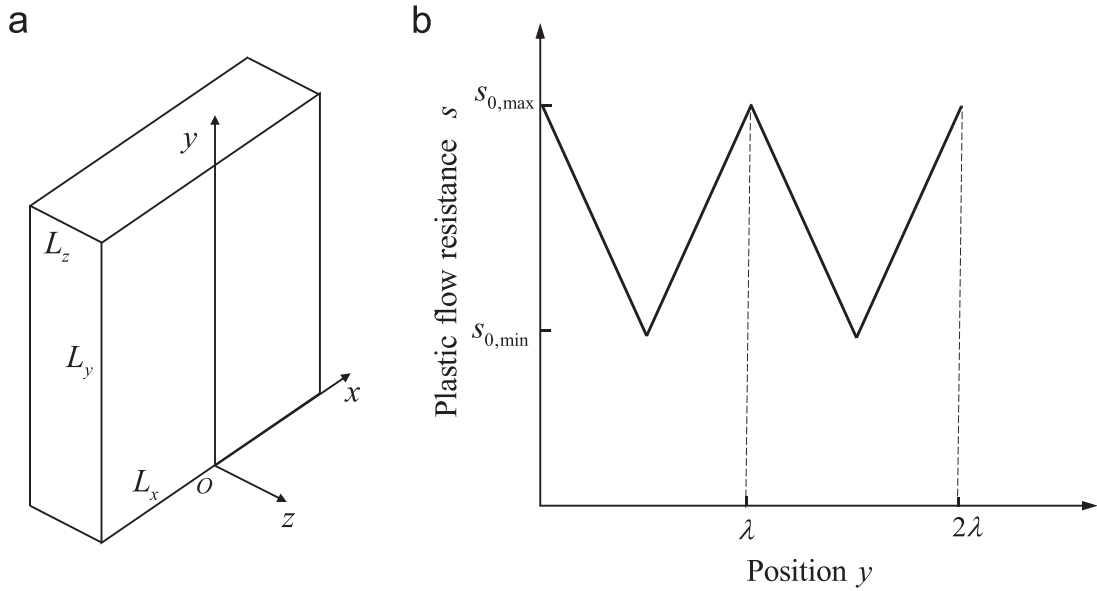
Fig. 2. GNT-1 to GNT-4 models. (a) A rectangular block is taken as a representative volume element of GNT Cu, with a gradient distribution of initial plastic flow resistance in the *x-y* cross section and under uniaxial tensile deformation along the *z*-axis. (b) A triangle wave profile of initial plastic flow resistance along *y*-axis, with the maximum resistance $s_{0,\max}$, minimum resistance $s_{0,\min}$ and wavelength λ.

as a dimensionless hardening rate magnification factor arising from plastic strain gradients. In addition, ε_2 and n_2 are used to control the range of $\bar{\varepsilon}^p$ where the hardening effect of plastic strain gradients is pronounced. That is, this hardening effect predominates when $\bar{\varepsilon}^p$ is less than ε_2, but it decays quickly as $\bar{\varepsilon}^p$ increases above ε_2. To quantitatively represent the hardening effects of both plastic strain and plastic strain gradient on GNT Cu, ε_2 is taken to be much smaller than ε_1; in addition, an appropriate κ is taken such that $\kappa\sqrt{\alpha}h_0$ is much larger than h_0. As a result, Eq. (7) captures a two-stage hardening response arising from plastic strain gradients in GNT Cu. Specifically, a characteristically high hardening rate on the order of $\kappa\sqrt{\alpha}h_0$ predominates when $\bar{\varepsilon}^p$ is less than ε_2, while a characteristically low hardening rate on the order of h_0 takes over when $\bar{\varepsilon}^p$ becomes greater than ε_2. This two-stage hardening is characteristic of the experimentally measured stress-strain response of GNT Cu (Cheng et al., 2018) and implies the following dislocation strengthening effects in gradient structures. In the first stage of hardening, geometrically necessary dislocations (GNDs) (Ashby, 1970) are quickly generated to accommodate the plastic strain gradients resulting from the built-in strength gradients. These GNDs give rise to high hardening rates at small strains, thus reflecting a strong strengthening effect of plastic strain gradients. In the second stage, hardening due to plastic strain gradients becomes saturated and thus switches to the conventional plastic strain hardening, leading to markedly reduced hardening rates at large strains.

4. Gradient plasticity in GNT Cu

To study the gradient plastic responses of GNT Cu under uniaxial tension, we set up GNT-1 to GNT-4 models with different strength gradients in Section 4.1. Considering the dominant axial stresses in these GNT models, we reduce the general 3D gradient theory into a 1D gradient theory in Section 4.2. This 1D theory is numerically implemented to simulate the tensile responses of GNT-1 to GNT-4 models, as described in Section 4.3. Numerical results are compared with experimental measurements in terms of the overall stress-strain responses of GNT-1 to GNT-4. Detailed analysis of numerical results for GNT-1 reveals the primary strengthening effects of gradient plasticity in GNT Cu.

4.1. GNT-1 to GNT-4 models

As shown in Fig. 2a, we consider a rectangular block, with the dimensions of $L_x \times L_y \times L_z$, as a representative volume element of GNT-1 to GNT-4 samples. The *z*-axis of the block is oriented along the tensile loading direction, and the *y*-axis is along the sample thickness direction. A gradient distribution of the initial plastic flow resistance $s(y, t = 0)$ (equivalent to initial tensile yield strength) is prescribed in the *x-y* cross section. Based on the experimentally measured hardness profiles of GNT-1 to GNT-4 samples (Fig. 1), triangle waves with different wavelengths and gradients are used to represent $s(y, t = 0)$ for GNT-1 to GNT-4 models. A typical triangle wave (Fig. 2b) is prescribed by three parameters: the maximum resistance $s_{0,\max}$, minimum resistance $s_{0,\min}$, and wavelength λ. To facilitate comparison between different GNT models, $s_{0,\max}$ is taken to be identical for GNT-1 to GNT-4 models and so is $s_{0,\min}$. Consider GNT-1 as an example. Its linear profile of $s^{GNT-1}(y, t = 0)$

corresponds to the half period of a triangle wave, $\lambda^{\text{GNT-1}}/2 = L_y = 400 \, \mu\text{m}$, and is expressed as

$$s^{\text{GNT-1}}(y, t = 0) = s_{0,\max} - g_s^{\text{GNT-1}} \cdot y \tag{9}$$

where $g_s^{\text{GNT-1}}$ is the gradient of the initial plastic flow resistance of GNT-1. For GNT-2 to GNT-4 models, their triangle wave profiles of $s(y, t = 0)$ have the same half period form as Eq. (9), but the respective g_s is increased to 2, 4 and 7 times $g_s^{\text{GNT-1}}$, and the respective λ is reduced to 1/2, 1/4 and 1/7 times $\lambda^{\text{GNT-1}}$.

4.2. 1D gradient theory of plasticity

Considering the fact that $s(y, t = 0)$ is only a function of coordinate y in GNT-1 to GNT-4 models, we assume all the stress and strain fields from uniaxial tension depend only on coordinate y and time t. We further assume that $\sigma_{zz}(y, t)$ is the only nonzero stress component. Compared to a full 3D stress analysis, this simplified 1D stress state facilitates a more physically transparent analysis of the primary strengthening effects of gradient plasticity. When a uniaxial stress state prevails, equilibrium is trivially satisfied. It follows that according to Eq. (4), the equivalent stress $\bar{\sigma}(y, t)$ is reduced to the axial stress $\sigma_{zz}(y, t)$; according to Eq. (3), the equivalent plastic strain rate $\dot{\bar{\varepsilon}}^{\text{p}}(y, t)$ is reduced to the axial strain rate $\dot{\varepsilon}_{zz}^{\text{p}}(y, t)$, such that the lateral strain rate is given by $\dot{\varepsilon}_{xx}^{\text{p}}(y, t) = \dot{\varepsilon}_{yy}^{\text{p}}(y, t) = -\dot{\bar{\varepsilon}}^{\text{p}}(y, t)/2$. Once $\sigma_{zz}(y, t)$ is solved, the average axial stress $\sigma_{zz}^{\text{avg}}(t)$ is obtained by

$$\sigma_{zz}^{\text{avg}}(t) = \frac{1}{L_y} \int_0^{L_y} \sigma_{zz}(y', t) \mathrm{d}y' \tag{10}$$

To evaluate $\sigma_{zz}^{\text{avg}}(t)$, we first solve for $\varepsilon_{zz}^{\text{p}}(y, t)$, $s(y, t)$ and $\sigma_{zz}(y, t)$ by time integration of their respective rate equations. In the present 1D gradient theory, the plastic strain rate in Eq. (5) is reduced to

$$\dot{\varepsilon}_{zz}^{\text{p}}(y, t) = \dot{\bar{\varepsilon}}_0^{\text{p}} \left(\frac{\sigma_{zz}(y, t)}{s(y, t)} \right)^{1/m} \tag{11}$$

The accumulated equivalent plastic strain $\bar{\varepsilon}^{\text{p}}(y, t)$ is given by $\bar{\varepsilon}^{\text{p}}(y, t) = \varepsilon_{zz}^{\text{p}}(y, t) = \int_0^t \dot{\varepsilon}_{zz}^{\text{p}}(y, t') \mathrm{d}t'$. The scalar measure of plastic strain gradients α in Eq. (8) is reduced to $\alpha = |\partial \bar{\varepsilon}^{\text{p}}(y, t)/\partial y|$. Then the hardening rate in Eq. (7) becomes

$$h(y, t) = \frac{h_0}{1 + \left(\bar{\varepsilon}^{\text{p}}/\varepsilon_1 \right)^{n_1}} \left[1 + \frac{\kappa \sqrt{\left| \partial \bar{\varepsilon}^{\text{p}}/\partial y \right|}}{1 + \left(\bar{\varepsilon}^{\text{p}}/\varepsilon_2 \right)^{n_2}} \right] \tag{12}$$

As discussed earlier, with an appropriate choice of material parameters, the hardening rate relation of Eq. (12) represents a two-stage hardening response of GNT Cu. That is, a high hardening rate on the order of $\kappa h_0 \sqrt{|\partial \bar{\varepsilon}^{\text{p}}/\partial y|}$ predominates when $\bar{\varepsilon}^{\text{p}}$ is less than ε_2, while a low high hardening rate on the order of h_0 predominates when $\bar{\varepsilon}^{\text{p}}$ is greater than ε_2. Once $\dot{\varepsilon}_{zz}^{\text{p}}(y, t)$ and $h(y, t)$ are known, the hardening rate $\dot{s}(y, t)$ is determined by $\dot{s}(y, t) = h(y, t)\dot{\varepsilon}_{zz}^{\text{p}}(y, t)$. Time integration of $\dot{s}(y, t)$ yields $s(y, t) = \int_0^t \dot{s}(y, t') \mathrm{d}t'$. Suppose the x-y cross section in Fig. 2a moves at a constant applied strain rate $\dot{\varepsilon}_{zz}^{\text{a}}$. The elastic strain rate along the z-axis is given by

$$\dot{\varepsilon}_{zz}^{\text{e}}(y, t) = \dot{\varepsilon}_{zz}^{\text{a}} - \dot{\varepsilon}_{zz}^{\text{p}}(y, t) \tag{13}$$

and the elastic strain rate in the lateral direction is given by $\dot{\varepsilon}_{xx}^{\text{e}} = \dot{\varepsilon}_{yy}^{\text{e}} = -\nu \dot{\varepsilon}_{zz}^{\text{e}}$. The axial stress rate is obtained by

$$\dot{\sigma}_{zz}(y, t) = E \dot{\varepsilon}_{zz}^{\text{e}}(y, t) \tag{14}$$

Time integration of $\dot{\sigma}_{zz}(y, t)$ yields $\sigma_{zz}(y, t) = \int_0^t \dot{\sigma}_{zz}(y, t') \mathrm{d}t'$. Finally, the average axial stress $\sigma_{zz}^{\text{avg}}(t)$ is obtained using Eq. (10).

4.3. Results

We numerically implement the 1D gradient theory in Section 4.2 to simulate the tensile response of GNT-1 to GNT-4 models. Suppose the x-y cross section of a GNT model moves at a constant applied strain rate $\dot{\varepsilon}_{zz}^{\text{a}}$ of $1 \times 10^{-3} \, \text{s}^{-1}$. We obtain the average axial stress $\sigma_{zz}^{\text{avg}}(t)$ versus applied tensile strain, $\varepsilon_{zz}^{\text{a}}(t) = \dot{\varepsilon}_{zz}^{\text{a}} t$, by explicit time integration of rate equations in Section 4.2. The integration time step is taken as $1 \times 10^{-3} \, \text{s}$. Eighty equally spaced integration points along the y-axis are used. The plastic strain gradient at each integration point is calculated by the central difference method.

It should be emphasized that special care should be taken when calculating the plastic strain gradients at both the free surface and at the end point of each half period. This is because outside the free surface, the plastic strain does not exist; and at the end point of each half period, the plastic strain gradient flips sign when calculated from either side of the end point. We find that the forward or backward difference method can give a stable, physically-sound numerical solution. In other words, at the surface of GNT samples, the plastic strain gradient at the material side of a free surface dictates the local hardening response; inside GNT samples, the plastic strain gradient at one side of the end point of each half period controls the local hardening response. In contrast, the central difference method gives a zero plastic strain gradient at the end point,

Table 1
Parameters used in both 1D and 3D gradient plasticity simulations.

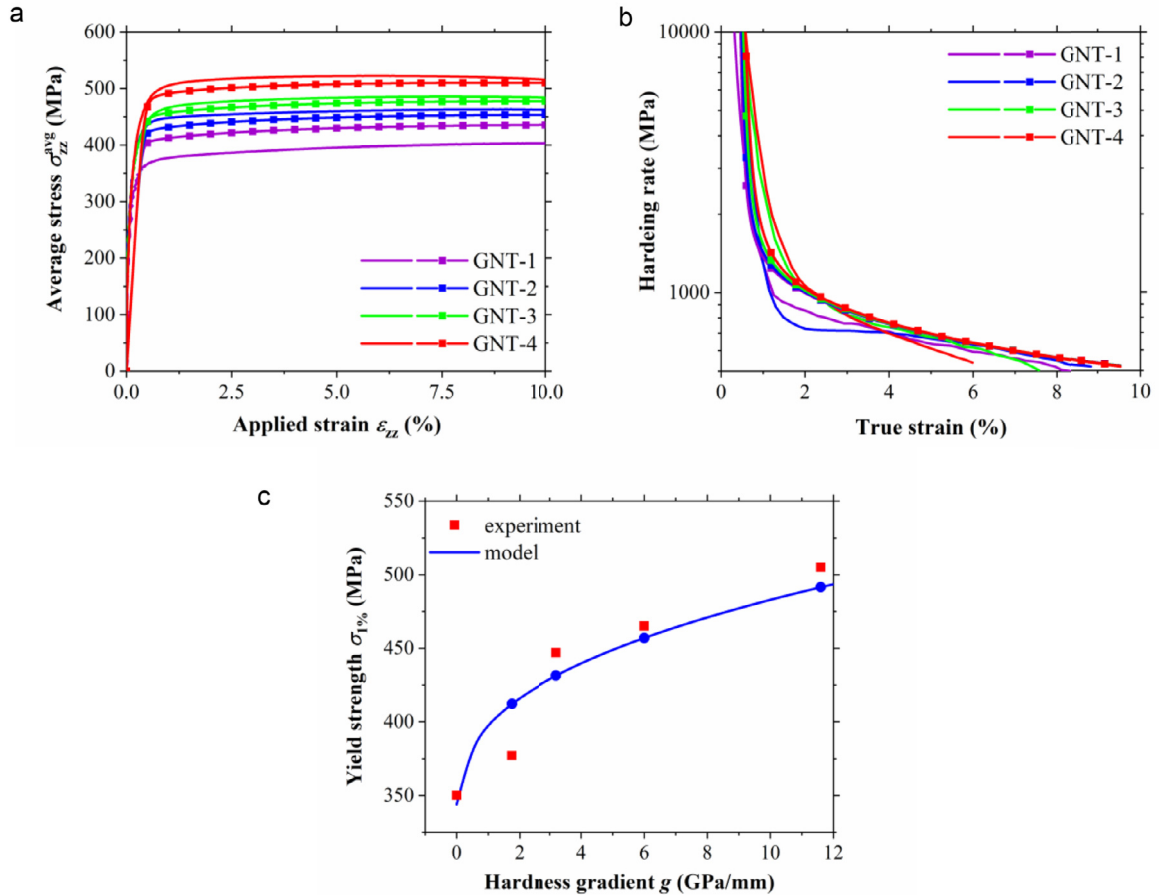| E(GPa)	ν	m	$\dot{\varepsilon}_0^p$ (s^{-1})	h_0(MPa)	ε_1	n_1	ε_2	n_2	$\kappa\,(\sqrt{\text{m}})$
124	0.3	0.001	0.001	2000	0.015	0.6	0.0001	2.0	139.7

Fig. 3. Comparison of experimental measurements (Cheng et al., 2018) and simulation results of uniaxial tension from the 1D gradient theory of plasticity. (a) Tensile engineering stress σ_{zz}^{avg} versus engineering strain ε_{zz}^a for GNT-1 to GNT-4 from experiments (solid lines) and simulations (solid lines with symbols). (b) Strain hardening rate $d\sigma_{zz}^{avg}/d\varepsilon_{zz}^a$ versus true strain for GNT-1 to GNT-4 from experiments (solid lines) and simulations (solid lines with symbols). (c) Sample-average yield strength $\sigma_{1\%}$ versus hardness gradient g for GNT-1 to GNT-4 from experiments (red squares) and simulations (blue dots). Also plotted is the predicted average yield strength $\sigma_{1\%}$ versus hardness gradient (blue curve) from additional simulations of 25 GNT models with increasing hardness gradient by equal increment. (For interpretation of the references to color in the text, the reader is referred to the web version of this article.)

resulting in an unstable, oscillating solution around the end point. We further find that a similar treatment of plastic strain gradients is needed for the nonlinear wave profile of initial plastic flow resistance, as to be discussed later. The material parameters used in our numerical simulations are listed in Table 1. They are determined by fitting the numerical results of the stress-strain responses of GNT-1 to GNT-4 models to the corresponding experimental stress-strain curves of GNT-1 to GNT-4 samples. Because of the small strain rate sensitivity m and low applied strain rate $\dot{\varepsilon}_{zz}^a$ used, our numerical results represent the rate-independent responses under quasi-static loading conditions. As such, the numerical results of stresses and strains are presented as functions of applied tensile strain ε_{zz}^a without explicit time dependence.

Fig. 3a shows the numerical results of the average tensile (engineering) stress σ_{zz}^{avg} versus applied tensile (engineering) strain ε_{zz}^a for GNT-1 to GNT-4 models, which reasonably agree with the corresponding experimental results. Fig. 3b shows the numerical results of the strain hardening rate $d\sigma_{zz}^{avg}/d\varepsilon_{zz}^a$ versus applied true strain for GNT-1 to GNT-4 models, which also reasonably agree with the corresponding experimental results. The experimental and simulated hardening rates clearly show the two-stage hardening response in GNT Cu, as discussed earlier in Section 3. Hence, the hardening rate relation of Eq. (7) can well capture the overall hardening response due to increasing plastic strain and plastic strain gradient. However, Eq. (7) is a relatively simple nonlinear relation and thus cannot capture all the fine features of the stress-strain responses in

experiments, such as the hardening rate plateau at the strain of about 2% in GNT-1 and GNT-2. Such plateaus near 2% strain in experiments suggest some special effect of gradient structures on the transition from the high to low hardening-rate stage in the experimental GNT samples, which warrant further experimental and modeling studies in the future.

For each GNT model, the sample-average yield strength is defined as the average tensile stress $\sigma_{zz}^{\mathrm{avg}}$ at $\varepsilon_{zz}^{\mathrm{a}} = 1\%$ and thus denoted as $\sigma_{1\%}$. In Fig. 3c, the predicted $\sigma_{1\%}$ values for GNT-1 to GNT-4 models (blue circles) are plotted as a function of hardness gradient g and they reasonably agree with the corresponding experimental results (red squares). It is seen that the predicted $\sigma_{1\%}$ for GNT-1 has a relatively large deviation from the corresponding experimental data point. This difference is mainly attributed to the constant strength gradient used in the GNT-1 model, while a few hardness plateaus, with nearly zero strength gradients, are present in the experimental GNT-1 sample (see Fig. 1b). These plateaus stem from non-gradient variations of nanotwin thickness (Cheng et al., 2018). It should be noted that the yield strength gradients g_s are prescribed for GNT-1 to GNT-4 models, while the hardness gradients g are measured for GNT-1 to GNT-4 samples in experiments. To compare the experimental and simulation results, we adopt the following protocol to convert g_s to g. That is, for GNT-1 to GNT-4 models, we use the experimental values of wavelength λ, maximum yield strength $s_{0,\max}$ and minimum yield strength $s_{0,\min}$; the latter two are measured from the nanotwinned samples without structural gradient (Cheng et al., 2018). As such, these parameters fix the respective g_s for GNT-1 to GNT-4 models. For example, the strength gradient for GNT-1 is a constant of $g_s^{\mathrm{GNT-1}} = 0.56$ GPa/mm. Cheng et al. (Cheng et al., 2018) showed that the tensile yield strength of a homogeneous nanotwinned sample with uniform twin thickness is approximately 1/3 times the corresponding micro-indentation hardness in a GNT sample with the same local twin thickness. Hence, we assume $g \approx 3g_s$ and thus obtain $g^{\mathrm{GNT-1}} = 1.68$ GPa/mm. As such, the simulation results of $\sigma_{1\%}$ versus g_s are converted to $\sigma_{1\%}$ versus g to directly compare with the corresponding experimental results.

In addition, we estimate the sample-average yield strength at zero hardness gradient, $\sigma_{1\%,g=0}$, from a rule-of-mixture average of yield strengths measured from four homogeneous nanotwinned samples without structural gradient, but with different uniform twin thicknesses (Cheng et al., 2018). Then we calculate the extra strength of the GNT-1 model as $\Delta\sigma_{1\%} = \sigma_{1\%} - \sigma_{1\%,g=0}$. The extra strengths $\Delta\sigma_{1\%}$ for the GNT-2 to GNT-4 models are calculated by the same definition. To further characterize the nonlinear functional dependence of $\sigma_{1\%}$ on g, we conduct additional simulations for 25 GNT models with increasing g from 0 to 12 GPa/mm by equal increment. The corresponding results of $\sigma_{1\%}$ versus g are plotted as the blue curve in Fig. 3c. By least squares regression analysis of the $\sigma_{1\%}$ versus g data points for these 25 GNT models, we find that the simulated extra strength $\Delta\sigma_{1\%}$ closely obeys

$$\Delta\sigma_{1\%} = \beta\sqrt{g} \tag{15}$$

where the coefficient β is fitted as $41.7\sqrt{\mathrm{MPa}\cdot\mu\mathrm{m}}$. This nonlinear relation between the extra strength and hardness gradient is reasonably supported by the experimental data (red squares), and it warrants further experimental validation by more GNT Cu samples with different structural gradients in the future. As to be discussed later, the relation between $\Delta\sigma_{1\%}$ and g in Eq. (15) originates from the hardening effect of plastic strain gradients in GNT Cu.

Our in-depth analysis of numerical results of GNT-1 to GNT-4 models reveals the primary features in plastically deformed gradient structures, including progressive yielding, gradient distributions of plastic strain and extra plastic flow resistance. Consider GNT-1 as an example. Fig. 4a shows the distributions of plastic flow resistance $s(\hat{y})$ along normalized $\hat{y}(= y/L_y)$ at different applied strains $\varepsilon_{zz}^{\mathrm{a}}$. The initial linear profile of $s(\hat{y})$ at $\varepsilon_{zz}^{\mathrm{a}} = 0$ corresponds to Eq. (9), with the maximum and minimum yield strength of 446 MPa and 223 MPa, respectively, giving a constant strength gradient $g_s = 0.56$ GPa/mm. As $\varepsilon_{zz}^{\mathrm{a}}$ increases to 0.25%, the soft region at large $\hat{y}$ becomes plastically yielded, while the hard region at small $\hat{y}$ remains elastic. Due to the hardening effects of both plastic strains and plastic strain gradients, $s(\hat{y})$ increases in the plastic region and exhibits a nonlinear profile represented by a black curved segment. In contrast, $s(\hat{y})$ remains unchanged in the elastic region and maintains a linear profile represented by a black straight segment. The location where the black curved and straight segments meet is the boundary between the elastic and plastic regions.

Fig. 4b shows the distribution of plastic strain $\varepsilon_{zz}^{\mathrm{p}}(\hat{y})$ (the black curve) when $\varepsilon_{zz}^{\mathrm{a}} = 0.25\%$. The plastic region with nonzero $\varepsilon_{zz}^{\mathrm{p}}(\hat{y})$ can be readily identified. A gradient distribution of plastic strain develops within the plastic region, such that $\varepsilon_{zz}^{\mathrm{p}}(\hat{y})$ has the largest value at $\hat{y} = 1$ and decreases to zero at the elastic-plastic boundary. It is interesting to observe that the plastic strain gradient $\alpha(\hat{y}) = |\partial\varepsilon_{zz}^{\mathrm{p}}/\partial y|$ is close to a constant. To understand this result, we note that during the early stage of progressive yielding, the stress $\sigma_{zz}(\hat{y})$ and thus $s(\hat{y})$ at $\varepsilon_{zz}^{\mathrm{a}} = 0.25\%$ are close to $s(\hat{y}, t = 0)$. Based on Eq. (13), a constant plastic strain gradient in the plastic region can be estimated as

$$\alpha(\hat{y}) \approx \left|\frac{\partial[\varepsilon_{zz}^{\mathrm{a}} - s(y, t = 0)/E]}{\partial y}\right| = \frac{g_s}{E} \tag{16}$$

Eq. (16) indicates that the plastic strain gradient $\alpha(\hat{y})$ is dictated by the built-in strength gradient g_s. But the calculated $\alpha(\hat{y})$ from the black curve in Fig. 4b is only about one third of g_s/E. This discrepancy is attributed to the nonlinear hardening responses at different $\hat{y}$ during the process of progressive yielding through sample thickness.

Fig. 4c shows the extra plastic flow resistance $\Delta s(\hat{y})$ defined as the difference of $s(\hat{y})$ with and without the hardening effect of plastic strain gradients, the latter of which is evaluated by setting $\kappa = 0$ in Eq. (12). Compared to the initial $s(\hat{y})$ at $\varepsilon_{zz}^{\mathrm{a}} = 0$, $\Delta s(\hat{y})$ is substantial, reaching the maximum of about 40 MPa at $\varepsilon_{zz}^{\mathrm{a}} = 0.25\%$. In addition, Fig. 4d shows the distribution of axial stress $\sigma_{zz}(\hat{y})$ at $\varepsilon_{zz}^{\mathrm{a}} = 0.25\%$. In the elastic region, $\sigma_{zz}(\hat{y})$ is constant, reflecting a uniform distribution of
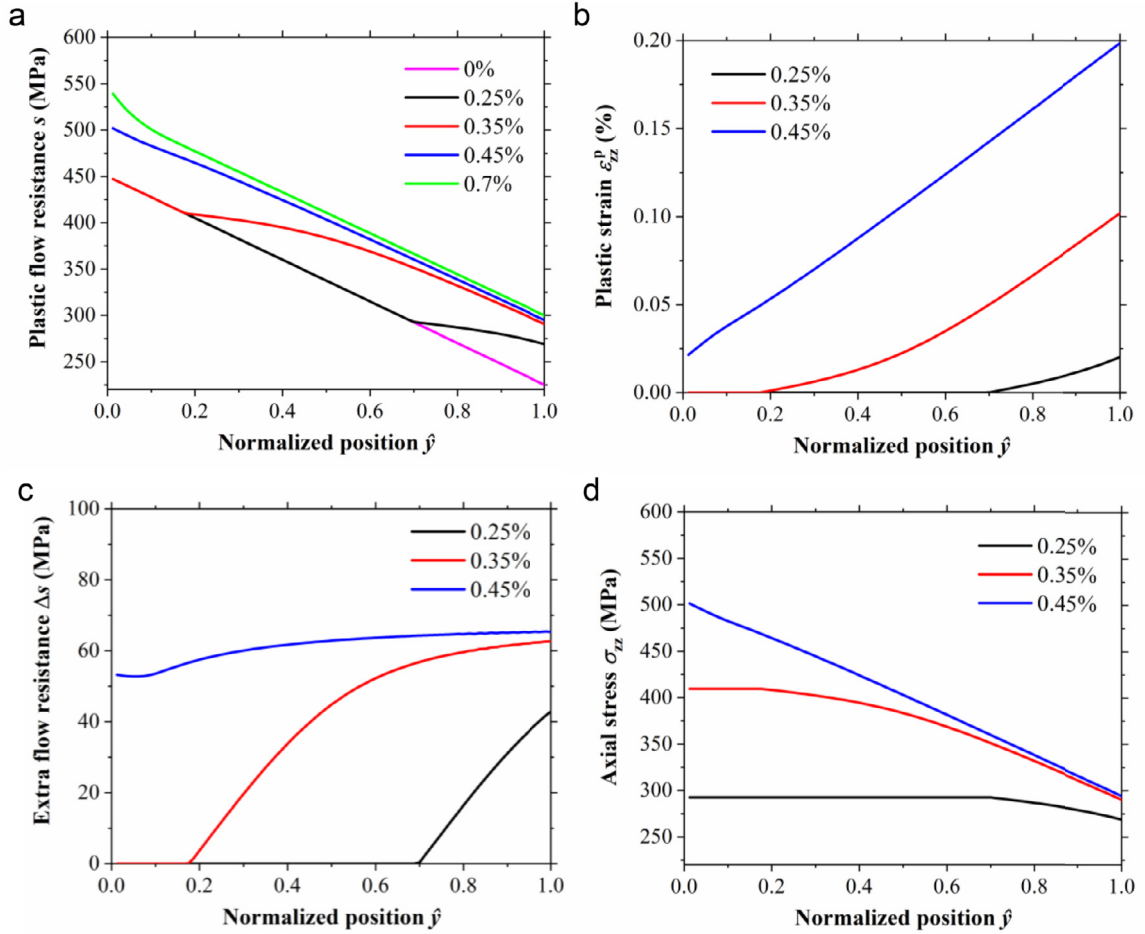
Fig. 4. Simulation results of the GNT-1 model at different applied tensile strains ε_{zz}^a from the 1D gradient theory of plasticity, showing the distributions of (a) plastic flow resistance $s(\hat{y})$, (b) plastic strain $\varepsilon_{zz}^p(\hat{y})$, (c) extra flow resistance $\Delta s(\hat{y})$, and (d) axial stress $\sigma_{zz}(\hat{y})$.

tensile elastic strain $\varepsilon_{zz}^e(\hat{y})$ equal to applied tensile strain ε_{zz}^a. In the plastic region, the nonlinear profile of $\sigma_{zz}(\hat{y})$ closely matches that of $s(\hat{y})$; $\sigma_{zz}(\hat{y})$ decreases from the elastic-plastic boundary to $\hat{y} = 1$, due to the increased plastic strain and decreased elastic strain with increasing $\hat{y}$.

To reveal the effects of increasing load, Fig. 4a shows that as ε_{zz}^a increases to 0.35%, $s(\hat{y})$ further increases in the plastic region and continues to exhibit a nonlinear profile as a red curved segment; $s(\hat{y})$ remains unchanged in the elastic region and thus maintains a linear profile as a red straight segment. Moreover, the plastic region expands, while the elastic region shrinks, such that the elastic-plastic boundary moves to smaller $\hat{y}$. This progressive yielding response is also evident in Fig. 4b, showing an increased plastic region with a concomitant increase of $\varepsilon_{zz}^p(\hat{y})$. As a result, the region with the gradient distribution of plastic strain expands. The plastic strain gradient $\alpha(\hat{y}) = |\partial \varepsilon_{zz}^p / \partial y|$ becomes close to g_s/E as estimated by Eq. (16). Fig. 4c shows $\Delta s(\hat{y})$ at $\varepsilon_{zz}^a = 0.35\%$. Compared to $s(\hat{y})$ at $\varepsilon_{zz}^a = 0.25\%$, the increase of $s(\hat{y})$ is primarily caused by the extra hardening effect of plastic strain gradients. In addition, Fig. 4d shows that in the shrinking elastic region, the constant $\sigma_{zz}(\hat{y})$ is elevated due to an increase of elastic strain; in the expanding plastic region, the nonlinear distribution of $\sigma_{zz}(\hat{y})$ follows that of $s(\hat{y})$ at $\varepsilon_{zz}^a = 0.35\%$.

When ε_{zz}^a reaches 0.45%, the progressive yielding process has completed, such that the entire cross section becomes plastically yielded. Fig. 4a shows that similar to $s(\hat{y})$ at $\varepsilon_{zz}^a = 0$, the distribution of $s(\hat{y})$ at $\varepsilon_{zz}^a = 0.45\%$ becomes almost linear again. This arises from the saturation of the extra hardening effect of plastic strain gradients, as to be further discussed next. Fig. 4b confirms that the plastic region occupies the entire cross section at $\varepsilon_{zz}^a = 0.45\%$; the plastic strain gradient $\alpha(\hat{y})$ is almost identical to g_s/E as estimated by Eq. (16). Fig. 4c shows $\Delta s(\hat{y})$ that varies weakly between 55-65 MPa. This $\Delta s(\hat{y})$ represents the limit of the extra hardening effect due to the plastic strain gradient in GNT-1. To understand this limit, we note that Eq. (7) and accordingly Eq. (12) represent a two-stage hardening behavior. Namely, the hardening rate is dominated by the plastic strain gradient when $\bar{\varepsilon}^p$ is less than ε_2 (= 0.0001) and decays quickly as $\bar{\varepsilon}^p$ increases above ε_2, thereby giving rise to the limit of $\Delta s(\hat{y})$ due to plastic strain gradients. When $\bar{\varepsilon}^p$ increases above ε_2 at the hardest region ($\hat{y} = 0$), $\Delta s(\hat{y})$ becomes saturated in the entire cross section, resulting in the saturation of the overall extra strength $\Delta \sigma_{1\%}$

from the plastic strain gradient as $\varepsilon^{\mathrm{a}}_{zz}$ approaches about 0.5% and beyond. Hence, the extra strength $\Delta\sigma_{1\%}$ as defined earlier provides an effective measure of the sample-level extra strength. In addition, during progressive yielding, the limit of $\Delta s(\hat{y})$ at different $\hat{y}$ is attained at different $\varepsilon^{\mathrm{a}}_{zz}$, but the limit value of $\Delta s(\hat{y})$ depends weakly on $\hat{y}$, resulting in a linear profile of saturated $s(\hat{y})$. Fig. 4d shows the nearly linear distribution of $\sigma_{zz}(\hat{y})$ at $\varepsilon^{\mathrm{a}}_{zz} = 0.45\%$, which follows the corresponding $s(\hat{y})$.

Fig. 4a also shows the representative distribution of $s(\hat{y})$ at a high load of $\varepsilon^{\mathrm{a}}_{zz} = 0.7\%$. The overall linear profile (the green curve) is maintained with slight nonlinearity near $\hat{y} = 0$. As $\varepsilon^{\mathrm{a}}_{zz}$ increases from 0.45% to 0.7%, the slight increase of $s(\hat{y})$ is primarily caused by the hardening effect of plastic strains instead of plastic strain gradients. This result represents the saturated distribution of $s(\hat{y})$ that prevails under large tensile strains, e.g., in the range of 0.5% ~ 10% covered by the stress-strain curve in Fig. 2a. In addition, the distributions of $\varepsilon^{\mathrm{p}}_{zz}(\hat{y})$ and $\sigma_{zz}(\hat{y})$ are very close to the corresponding distributions at $\varepsilon^{\mathrm{a}}_{zz} = 0.45\%$ with slight increase, while $\Delta s(\hat{y})$ remains unchanged. Similar to the case of $\varepsilon^{\mathrm{a}}_{zz} = 0.45\%$, the sample average of $\Delta s(\hat{y})$ at $\varepsilon^{\mathrm{a}}_{zz} = 0.7\%$ also approaches the extra strength $\Delta\sigma_{1\%}$.

For GNT-2 to GNT-4 models, the corresponding numerical results show that all the half-period profiles of plastic flow resistance $s(\hat{y})$, tensile plastic strain $\varepsilon^{\mathrm{p}}_{zz}(\hat{y})$, extra flow resistance $\Delta s(\hat{y})$ and tensile stress $\sigma_{zz}(\hat{y})$ show qualitatively similar trends as GNT-1. However, due to the increasing strength gradient, the plastic strain gradient $\alpha(\hat{y})$ and extra flow resistance $\Delta s(\hat{y})$ become increasingly stronger from GNT-2 to GNT-4, leading to the increasing sample-level yield strength $\sigma_{1\%}$ and thus increasing sample-level extra strength $\Delta\sigma_{1\%}$.

5. Gradient plasticity finite element (GPFE) simulations

5.1. Method

To gain a complete understanding of the tensile responses of GNT-1 to GNT-4, we numerically implement the 3D gradient plasticity theory in ABAQUS/Explicit and perform finite element simulations for the 3D models of GNT-1 to GNT-4. We choose the classical rate-independent plasticity model in ABAQUS/Explicit with the Mises isotropic yield surface and associated plastic flow rule. Explicit time integration is used to simplify numerical calculations of plastic strain gradients and associated field variables. That is, the hardening rate relation of Eq. (12) is implemented by writing user subroutines VUSDFLD and VUHARD (ABAQUS/Explicit, 2016). At the end of each time increment, VUSDFLD is used to calculate the gradient of equivalent plastic strain within each element with the finite difference method; VUHARD is used to calculate the hardening response due to both plastic strain and plastic strain gradient; and then the updated plastic flow resistance s and hardening rate h are passed into ABAQUS/Explicit. The combined use of VUSDFLD and VUHARD provides a relatively simple method for 3D calculations of plastic strain gradients, as opposed to other VUMAT or UEL-based methods in ABAQUS (Lele and Anand, 2008, 2009). The 3D finite element models of GNT-1 to GNT-4 are constructed in ABAQUS/CAE (ABAQUS/Explicit, 2016). Each GNT model has a thin-slice geometry of $400\,\mu\mathrm{m} \times 400\,\mu\mathrm{m} \times 50\,\mu\mathrm{m}$ (corresponding to the schematic in Fig. 2a) and contains 4096 brick elements with full integration (C3D8). Eight integration points in each brick element facilitate a direct finite-difference calculation of plastic strain gradient within each element via VUSDFLD. To simulate uniaxial tension, we prescribe the following boundary conditions: the velocity along the z-direction is 0.4 nm/s on the right side of the x-y surface; the displacement in the z-direction is fixed on the opposite side of the x-y surface; other surfaces are traction free. For each GNT model, the initial distribution of yield strengths is assigned according to the same triangle wave profile as the corresponding 1D model in Section 4. The material parameters listed in Table 1 are also used in GPFE simulations.

5.2. Results

The GPFE simulation results of GNT-1 to GNT-4, including the overall tensile stress-strain curves and the axial stress and strain distributions in the cross section, agree closely with the corresponding 1D simulation results described in Section 4.2. Next, we focus on the GPFE simulation results of stress components neglected in the 1D gradient theory and simulations.

Consider GNT-1 as an example. We first present the 3D finite element simulation results without considering the extra hardening effect of plastic strain gradients. These results, as shown in Fig. 5, are obtained by setting $\kappa = 0$ in Eq. (7). They serve to validate the simplification used to derive the 1D gradient theory, namely, the stress components other than $\sigma_{zz}(x, y)$ are negligible. Fig. 5a shows the contour plot of $\sigma_{zz}(x, y)$ in the x-y cross section at $\varepsilon^{\mathrm{a}}_{zz} = 0.25\%$. The contour with red color corresponds to a nearly constant tensile stress $\sigma_{zz}(x, y)$ associated with elastic deformation, while the contour with varying colors other than red shows a gradient distribution of $\sigma_{zz}(x, y)$ resulting from progressive yielding. The elastic-plastic boundary is located at the transition layer between the red and yellow contours. These results are consistent with those from the 1D gradient theory, i.e., the black curve in Fig. 4a.

Fig. 5b and 5c show the contour plots of the shear stress $\sigma_{yx}(x, y)$ and normal stress $\sigma_{xx}(x, y)$ at $\varepsilon^{\mathrm{a}}_{zz} = 0.25\%$, respectively. First of all, it is seen that these stress components are much smaller than the corresponding axial stress $\sigma_{zz}(x, y)$ (Fig. 5a), thus validating the 1D gradient theory. Moreover, $\sigma_{yx}(x, y)$ and $\sigma_{xx}(x, y)$ exhibit non-uniform distributions in both x and y directions. These non-axial stresses arise due to the gradient structure and associated gradient strength in the GNT-1 model. At any moment of a progressive yielding process, the axial stress σ_{zz} and accordingly axial strain ε_{zz} (including both elastic and plastic components) vary with coordinate y, resulting in the varying lateral contraction ε_{xx} with y, irrespective of different Poisson's effects on the elastic and plastic parts of the axial strain. Accommodation of the varying ε_{xx} with y (i.e.,
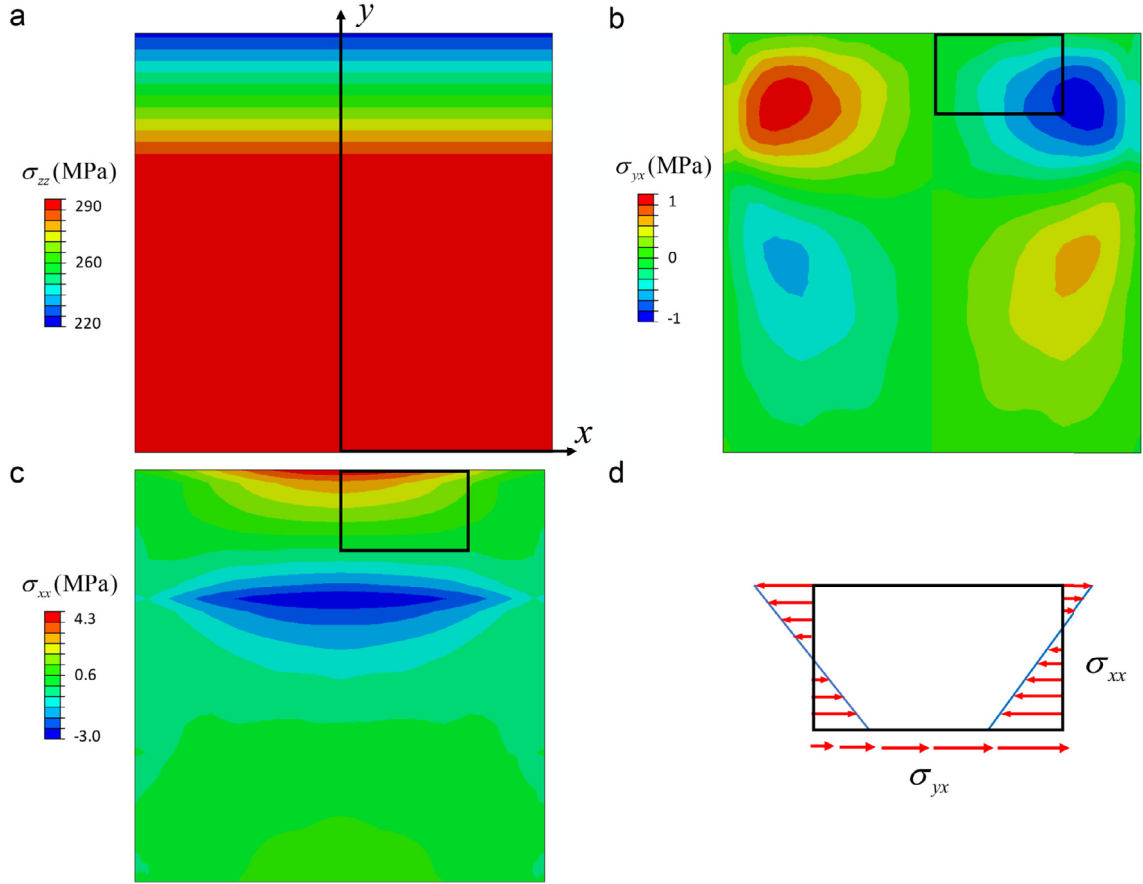
Fig. 5. 3D finite element simulation results of the GNT-1 model without accounting for the extra hardening effect of the plastic strain gradient. At the applied tensile strain of $\varepsilon_{zz}^a = 0.25\%$, plotted are the distributions of (a) axial stress $\sigma_{zz}(x, y)$, (b) lateral shear stress $\sigma_{yx}(x, y)$ and (c) lateral normal stress $\sigma_{xx}(x, y)$. (d) Equilibrium analysis of the non-uniform stresses $\sigma_{yx}(x, y)$ and $\sigma_{xx}(x, y)$ acting on a rectangle area in the *x-y* cross section as marked in (b) and (c); only stress components relevant to equilibrium in the *x*-direction are plotted as red arrows. (For interpretation of the references to color in the text, the reader is referred to the web version of this article.)

maintaining displacement continuity) gives rise to the non-zero shear stress $\sigma_{yx}(x, y)$. This further leads to other non-zero stress components such as $\sigma_{xx}(x, y)$, so as to maintain equilibrium along the *x*-direction. It is interesting to note that while the axial stress σ_{zz} only varies with *y*, $\sigma_{xx}(x, y)$ varies with both *x* and *y*. This is because $\sigma_{xx}(x, y)$ must self-equilibrate within any *x-z* plane, due to the absence of applied load in the *x*-direction. The same reasoning is applicable to the cause of a non-uniform distribution of $\sigma_{yx}(x, y)$ with both *x* and *y*. As an illustration, Fig. 5d shows the non-uniform $\sigma_{yx}(x, y)$ and $\sigma_{xx}(x, y)$ acting on the sides of a rectangular block (as marked in Fig. 5b and 5c), and these non-uniform stresses give a zero resultant force in the *x*-direction and thus satisfy the equilibrium condition.

Next, we present the GPFE simulation results that account for the extra hardening effect of plastic strain gradients by using the κ value in Table 1. Fig. 6a-c show the contour plots of $\sigma_{zz}(x, y)$, $\sigma_{yx}(x, y)$ and $\sigma_{xx}(x, y)$ in the *x-y* cross section of GNT-1 at $\varepsilon_{zz}^a = 0.25\%$. Compared to Fig. 5a, Fig. 6a shows that the extra hardening of plastic strain gradients causes an increase of the minimum axial stress $\sigma_{zz}(x, y)$ by about 50 MPa. However, compared with Fig. 5b-c, Fig. 6b-c show that the extra hardening does not lead to significant changes of $\sigma_{yx}(x, y)$ and $\sigma_{xx}(x, y)$. As a result, $\sigma_{yx}(x, y)$ and $\sigma_{xx}(x, y)$ are still much lower than $\sigma_{zz}(x, y)$ when the extra hardening effect is accounted for. In addition, Fig. 6d shows that the predicted tensile stress-strain curves are nearly identical between 1D and 3D simulations for GNT-1. Hence, the combined 3D finite element simulation results in Figs. 5 and 6 quantitatively demonstrate that the axial stress dominates over other stress components in GNT Cu under uniaxial tension.

6. Discussion

6.1. Optimization of gradient structures toward the maximum strength

Insights from the above gradient plasticity simulations can be applied to optimize the gradient structures and associated gradient strengths in a GNT-D(esign) model toward achieving the maximum sample-average strength. For the GNT-D model,
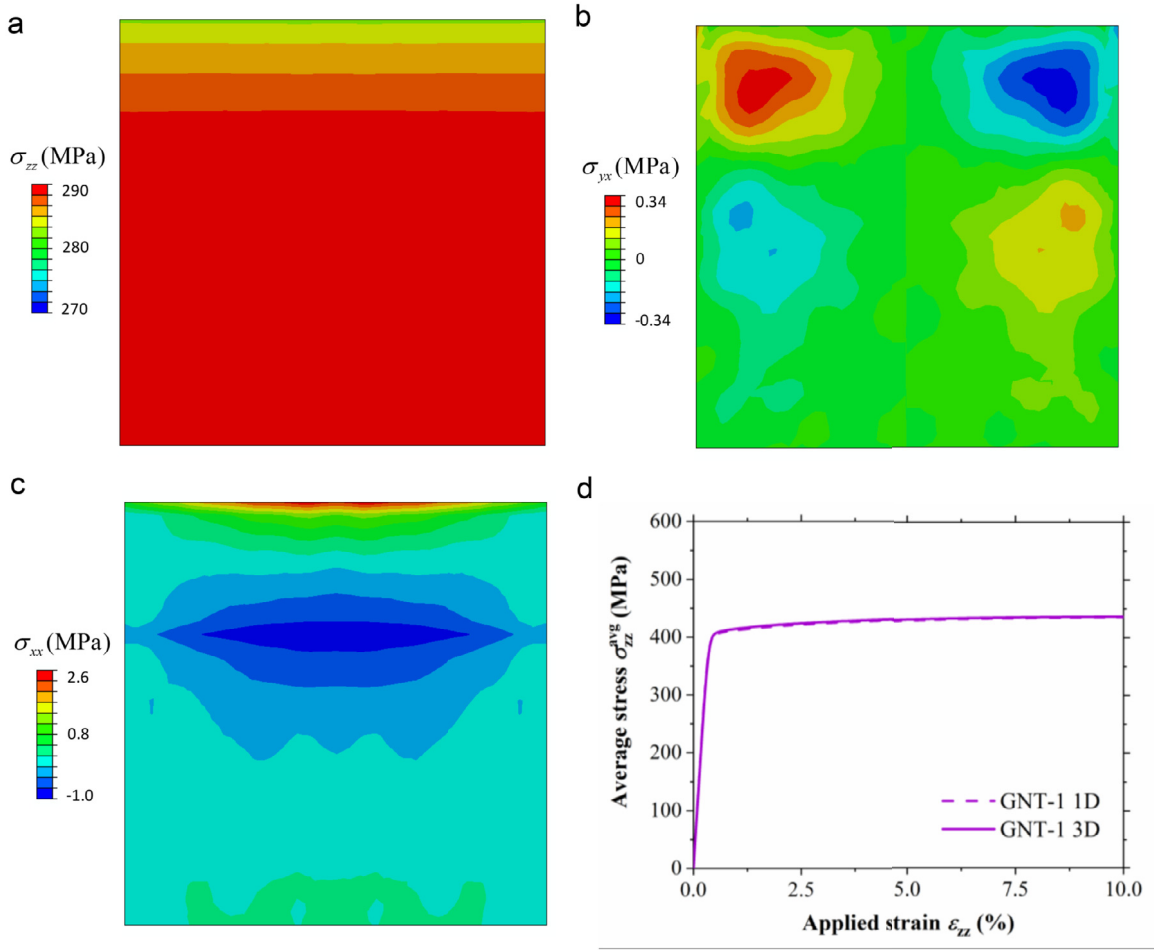
Fig. 6. 3D finite element simulation results of the GNT-1 model accounting for the extra hardening effect of plastic strain gradients. At the applied tensile strain of $\varepsilon_{zz}^a = 0.25\%$, plotted are the distributions of (a) axial stress $\sigma_{zz}(x, y)$, (b) lateral shear stress $\sigma_{yx}(x, y)$, and (c) lateral normal stress $\sigma_{xx}(x, y)$. (d) Comparison of the tensile stress-strain curves between 1D and 3D simulations.

we consider a family of triangle-wave strength distributions as in Fig. 2b. Given the initial plastic flow resistance $s(y, t = 0)$ of the GNT-D model, its sample-average plastic resistance s_{avg} at $\varepsilon_{zz}^a = 1\%$ can be expressed as

$$s_{avg} = \bar{s} + \overline{\Delta s} \tag{17}$$

where $\bar{s}$ is the rule-of-mixture average of $s(y, t = 0)$ through the cross section and becomes $\bar{s} = (s_{0,max} + s_{0,min})/2$ for the triangle wave profile of $s(y, t = 0)$; $\overline{\Delta s}$ is the sample-average extra flow resistance arising from plastic strain gradients. In the current rate-independent model, s_{avg} corresponds to the sample-average yield strength $\sigma_{1\%}$. According to Fig. 3b and Eq. (15), $\overline{\Delta s}$ is approximately represented by $\overline{\Delta s} = \beta\sqrt{g} = \beta_s\sqrt{g_s}$, where g_s is the gradient of the initial plastic flow resistance and given by $g_s = (s_{0,max} - s_{0,min})/(\lambda/2)$ for the triangle wave profile of $s(y, t = 0)$; the coefficient β_s is given by $\beta_s = \sqrt{g/g_s}\beta = \sqrt{3}\beta = 72.2\sqrt{\text{MPa} \cdot \mu\text{m}}$. Thus, Eq. (17) becomes

$$s_{avg} = \frac{s_{0,max} + s_{0,min}}{2} + \beta_s\sqrt{\frac{s_{0,max} - s_{0,min}}{\lambda/2}} \tag{18}$$

Based on Eq. (18), s_{avg} can be optimized in the parameter space of $\{s_{0,max}, s_{0,min}, \lambda\}$ for the GNT-D model. Generally speaking, certain regions in the parameter space may not be accessible due to constraints from material processing; moreover, when certain parameters reach their achievable limits, s_{avg} has to be optimized in a reduced parameter space. Three scenarios of optimization are considered under the aforementioned constraints. First, we note that s_{avg} increases monotonically with increasing $s_{0,max}$, when both $s_{0,min}$ and λ are fixed. This is because both $\bar{s}$ and $\overline{\Delta s}$ increase with $s_{0,max}$. For nanotwinned Cu, reducing twin thickness can raise $s_{0,max}$. However, it is difficult to keep reducing twin thickness by a specific processing method such as electrodeposition (Cheng et al., 2018), so that s_{avg} is limited by the achievable value of
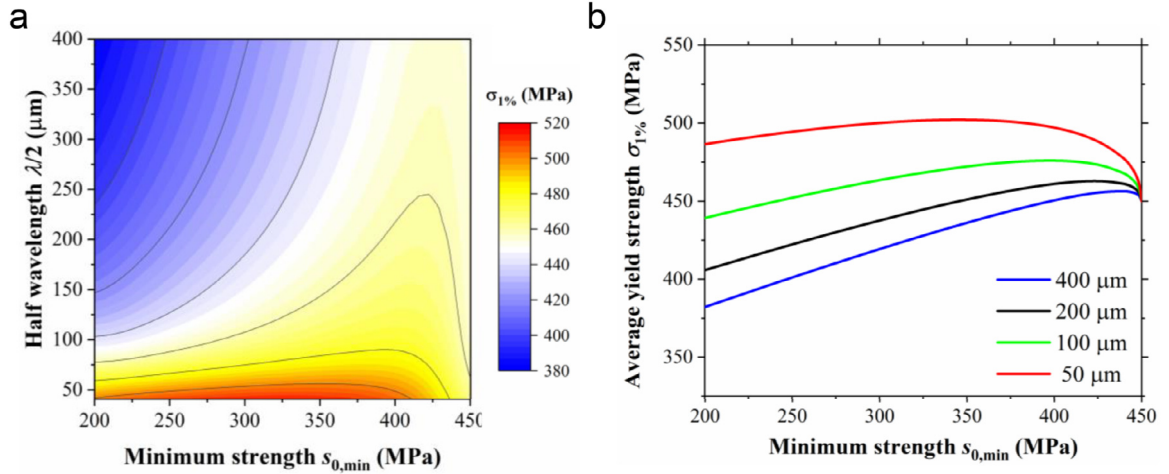
Fig. 7. Optimization of the average plastic flow resistance s_{avg} by tuning $s_{0,min}$ and λ, while holding $s_{0,min}$ fixed. (a) Contour plot of $\sigma_{1\%}$ ($\approx s_{avg}$) for GNT-D in the parameter space of $\{s_{0,min}, \lambda/2\}$, when $s_{0,max}$ is fixed at 446 MPa. (b) $\sigma_{1\%}$ versus $s_{0,min}$ curves extracted from (a) for several representative half periods $\lambda/2$.

$s_{0,max}$. Second, s_{avg} increases monotonically by reducing λ, when both $s_{0,min}$ and $s_{0,max}$ are fixed. In this case, as λ decreases, $\overline{\Delta s}$ increases, while $\bar{s}$ remains unchanged. Similarly, it is difficult to keep reducing λ by a specific processing method.

The third scenario involves a non-monotonic change of s_{avg}, thus requiring a search of the optimal parameter(s). For example. s_{avg} can be optimized by tuning $s_{0,min}$, when $s_{0,max}$ and λ are fixed. This is because increasing $s_{0,min}$ raises $\bar{s}$, but lowers $\overline{\Delta s}$ due to decreasing g_s. These two opposite effects can be optimized to achieve the maximum s_{avg}. As a more general example with two tunable parameters, Fig. 7a shows the contour plot of $\sigma_{1\%}$ (equal to s_{avg}) for GNT-D in the parameter space of $\{s_{0,min}, \lambda/2\}$, when $s_{0,max}$ is fixed at 446 MPa, which is the highest local yield strength in the GNT-4 model. Note that we use the model values of $s_{0,max}$ and $s_{0,min}$ instead of the experimental data since statistical variations of the latter can obscure the trend. It is seen from Fig. 7a that the maximum $\sigma_{1\%}$ occurs at the smallest $\lambda/2$ and intermediate $s_{0,min}$, consistent with the earlier discussion. From Fig. 7a, the $\sigma_{1\%}$ versus $s_{0,min}$ curves are extracted for several representative values of $\lambda/2$, as shown in Fig. 7b. In these curves, $\sigma_{1\%}$ invariably exceeds $s_{0,max}$, which is the strength of the strongest component of the GNT-D model; moreover, the non-monotonic change of $\sigma_{1\%}$ with $s_{0,min}$ becomes more pronounced as $\lambda/2$ is 100 μm or smaller. For $\lambda/2 = 50$ μm (as in the GNT-4 model), the corresponding peak value of $\sigma_{1\%}$ is 502 MPa when $s_{0,min} = 350$ MPa. This optimized strength for the GNT-D model exceeds $\sigma_{1\%} = 490$ MPa for the GNT-4 model with $s_{0,min} = 223$ MPa. The above study indicates that the strength of the experimental GNT-4 sample (Cheng et al., 2018) would become higher if its $s_{0,min} = 223$ MPa were to move to around $s_{0,min} = 350$ MPa.

6.2. Plastic strain gradient

An important insight from the 1D gradient plasticity simulation results in Section 4.3 is that the plastic strain gradient $\alpha(\hat{y})$ in GNT Cu is dictated by the built-in strength gradient, and it approaches a saturated value of about $g_s/E = g/3E$ throughout the sample cross section once progressive yielding is finished. This insight is further confirmed by Fig. 8, where the blue line corresponds to the saturated plastic strain gradient $\alpha_{1\%}$ obtained from 25 GNT models with increasing hardness gradient g between 0 and 12 GPa/mm by equal increment. Also shown in Fig. 8 is the theoretical prediction of $\alpha_{1\%} = g/3E$ (black line). Close agreement between the numerical results and theoretical predictions indicates that despite the extra strengthening effect of plastic strain gradients, the saturated plastic strain gradient, $\alpha_{1\%}$, is given approximately by $g_s/E = g/3E$. Based on Eq. (15), the extra strength $\Delta\sigma_{1\%}$ can be expressed in terms of the saturated plastic strain gradient $\alpha_{1\%}$,

$$\Delta\sigma_{1\%} = \gamma\sqrt{\alpha_{1\%}} \tag{19}$$

where the prefactor γ is $\beta\sqrt{3E}$. Hence, Eq. (19) reveals a direct functional relation between the extra strength and saturated plastic strain gradient in GNT Cu.

According to Ashby (Ashby, 1970), the plastic strain gradient α depends on the density of GNDs ρ_g by $\alpha = \rho_g b$, where b is the Burgers vector length. Then Eq. (19) can be rewritten as $\Delta\sigma_{1\%} = \gamma\sqrt{\rho_{g,1\%}b}$, where $\rho_{g,1\%}$ is ρ_g at $\varepsilon_{zz}^a = 1\%$. From the simulation results of $\alpha_{1\%}$ for GNT-1 to GNT-4, we can estimate the corresponding $\rho_{g,1\%} = \alpha_{1\%}/b$. Consider GNT-3 as an example. The corresponding $\alpha_{1\%}$ is about 17/m (Fig. 8). When b is taken as 2×10^{-10}m, $\rho_{g,1\%}$ is estimated as about 10^{11}/m^2. On the other hand, we can estimate the density of extra GNDs in GNT-3 (compared to the homogeneous nanotwinned structure without twin gradients) in terms of the bundles of concentrated dislocations (BCD), which are only observed in GNT samples but not in homogeneous nanotwinned samples with uniform twin thickness (Cheng et al., 2018). From
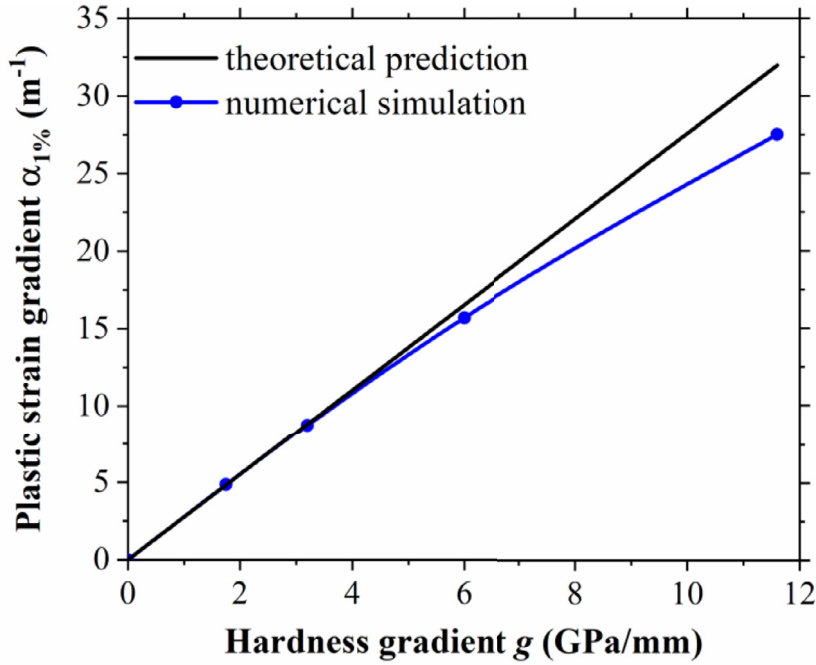
Fig. 8. Numerical simulation results of saturated plastic strain gradient $\alpha_{1\%}$ at $\varepsilon^a_{zz} = 1\%$ for 25 GNT models with increasing g from 0 to 12 GPa/mm (blue curve), as compared with the theoretical prediction from $\alpha_{1\%} = g/3E$ (black line). Blue dots correspond to numerical simulation results of GNT-1 to GNT-4. (For interpretation of the references to color in the text, the reader is referred to the web version of this article.)

the diffraction measurement of lattice misorientation across the BCD, we determine the density of local GNDs. Since the BCD only occupies a small fraction of grain volume, we further estimate the density of grain-average GNDs via the rule of mixture and take the result as the density of extra GNDs in GNT-3, which has the same order of magnitude as the above theoretical estimate of $\rho_{g,1\%}$ about $10^{11}/m^2$. Hence, our preliminary study suggests that the extra GNDs arising from gradient nanotwins can induce the extra strength for GNT Cu. Further in-depth study is underway towards elucidating the origin of generation of BCDs in GNT samples, as well as the impact of extra GNDs on the extra strength of GNT Cu, through quantitative characterization of back stresses (Mughrabi, 2006). The combined experimental and modeling results will be reported in a future paper.

6.3. Nonlinear strength distribution

To study the nonlinear distributions of initial plastic flow resistances, we revise the GNT-1 and GNT-4 models by replacing their triangle wave profiles of $s(y, t = 0)$ with sinusoidal wave profiles, while keeping the corresponding $s_{0,\max}$, $s_{0,\min}$ and λ unchanged. As a result, the strength gradient becomes a nonlinear function of coordinate y in each sinusoidal wave profile, in contrast to a constant magnitude of strength gradient in each triangle wave profile. For example, the initial plastic flow resistance of the revised GNT-1 model is represented by the half period of a sinusoidal wave

$$s(y, t = 0) = s_{0,\max} - (s_{0,\max} - s_{0,\min}) \sin\left(\frac{\pi}{\lambda} y\right) \tag{20}$$

where the wavelength λ is $2L_y$.

We numerically implement the 1D gradient theory for the revised GNT-1 to GNT-4 models, with the same numerical procedure as for the triangle wave profiles of $s(y, t = 0)$. As discussed earlier, special attention should be paid to the finite difference calculation of the plastic strain gradient. For a nonlinear sinusoidal wave profile, the plastic strain gradient is initially zero at the end point of a half period, but becomes non-zero with progressive yielding. As a result, the plastic strain gradient calculated from either side of the end point begins to flip sign as the integration time increases, leading to an unable, oscillating solution around the end point. We find that the forward or backward difference method can give a stable, physically-sound numerical solution, similar to the cases of triangle wave profiles.

The numerical results of the revised GNT-1 to GNT-4 models are close to the corresponding GNT-1 to GNT-4 models with the triangle wave profiles of $s(y, t = 0)$. As an example, Fig. 9 shows the cross-sectional distributions of plastic flow resistance $s(\hat{y})$ at different applied tensile strains ε^a_{zz} for the revised GNT-1 model with $s(y, t = 0)$ given by Eq. (20). Comparing with the results in Fig. 4a, the difference in $s(\hat{y})$ at the same ε^a_{zz} is small between the linear and nonlinear distributions of
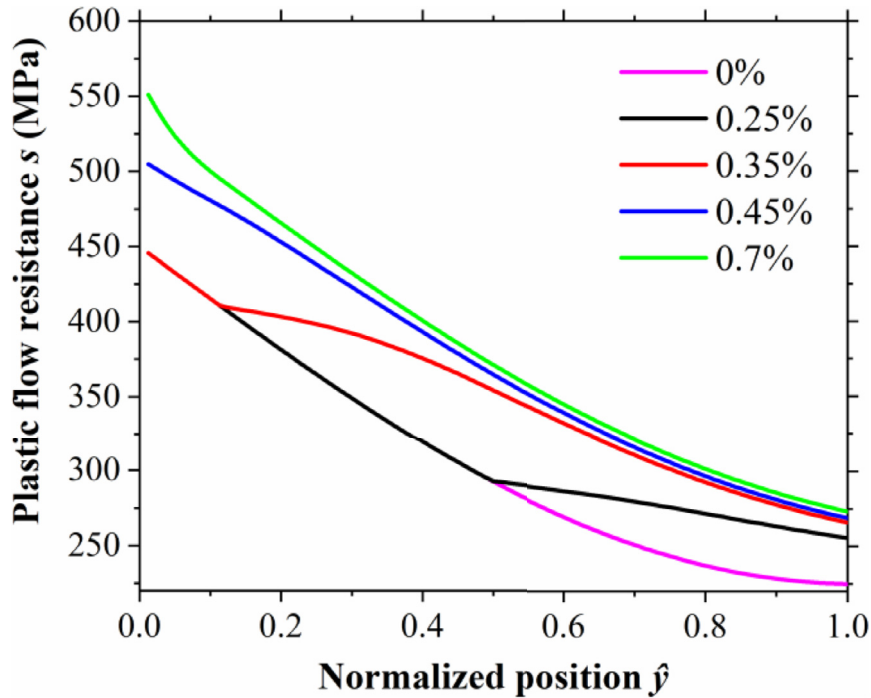
Fig. 9. Simulation results of the revised GNT-1 model with a sinusoidal wave profile of initial plastic flow resistance from the 1D gradient theory of plasticity, showing the cross-sectional distribution of plastic flow resistance $s(\hat{y})$ under different applied tensile strains ε_{zz}^{a}.

$s(y, t = 0)$. Overall, all the results obtained from the triangle wave profiles of $s(y, t = 0)$ are close to those from the nonlinear sinusoidal wave profiles with identical $s_{0,\max}$, $s_{0,\min}$ and λ.

7. Concluding remarks

We have developed a 3D gradient theory of plasticity by incorporating the strengthening effect of plastic strain gradients into the classical J_2 flow theory. Numerical simulations based on a simplified 1D gradient theory show the primary effects of gradient plasticity on GNT Cu under uniaxial tension, including progressive yielding, gradient distributions of plastic strain and extra flow resistance. We find that the extra strength $\Delta\sigma_{1\%}$ depends on the hardness gradient g (equivalent to 3 times the strength gradient g_s) by Eq. (15), and the saturated plastic strain gradient, $\alpha_{1\%}$, is approximately given by $g_s/E = g/3E$, as shown in Fig. 8. As a result, the extra strength depends on the saturated plastic strain gradient $\alpha_{1\%}$ by Eq. (19). Results from 3D gradient plasticity finite element simulations confirm 1D numerical results and further reveal 3D distributions of non-axial stresses despite their negligible role in the overall tensile response of GNT Cu. Predictions of the optimal gradient structures and associated gradient strength distributions suggest possible routes for achieving the maximum strength by tuning gradient nanostructures in GNT Cu. Altogether, our work provides an effective lower-order gradient theory of plasticity for gradient structured metals. The simulation results from this theory enable a quantitative understanding of the strain gradient plasticity effects on the strengthening of materials with gradient structures.

While the present work has established a direct relationship between the built-in structural gradient and resultant plastic strain gradient in GNT Cu, future studies are needed to elucidate the mechanistic origin of the extra strength arising from plastic strain gradients. This requires a combined experimental and modeling effort to address several fundamental questions, including how GNDs originate from built-in structural gradients and resulting plastic strain gradients, and why BCDs can uniquely develop in gradient structures, leading to the extra strength in GNT Cu. In addition, it remains to be established how the strengthening effect arises from plastic strain gradients through a dislocation density based model, and it is also necessary to explicitly account for the strain gradient effects originating from the internal interfaces of twin boundaries and grain boundaries and their spacings (Aifantis et al., 2006). We note that the current 3D finite element model, with calibration and improvement, may predict the tensile failure, i.e., ductility, of GNT samples. To this end, it is necessary to perform a combined experimental and modeling study of the initiation and growth of plastic strain localization in GNT samples in the future. Broadly, since GNT Cu represents a unique class of heterogeneous nanostructures with a high tunability of structural gradients, resolving the above issues may open opportunities of tailoring the structural heterogeneities in a variety of heterogeneous nanostructured materials (Ma and Zhu, 2017) for achieving outstanding mechanical properties.

Declaration of Competing Interest

The authors declare that they have no known competing financial interests or personal relationships that could have appeared to influence the work reported in this paper.

CRediT authorship contribution statement

Yin Zhang: Conceptualization, Methodology, Investigation, Software, Writing - original draft. **Zhao Cheng:** Methodology, Investigation, Writing - review & editing. **Lei Lu:** Supervision, Writing - review & editing. **Ting Zhu:** Supervision, Conceptualization, Writing - original draft, Writing - review & editing.

Acknowledgments

References

ABAQUS/Explicit, 2016. User's Manual. SIMULIA, Providence, R.I.

Aifantis, E.C., 1984. On the microstructural origin of certain inelastic models. J. Eng. Mater. Technol.-Trans. ASME 106, 326–330.

Aifantis, K.E., Soer, W.A., De Hosson, J.T.M., Willis, J.R., 2006. Interfaces within strain gradient plasticity: theory and experiments. Acta Mater. 54, 5077–5085.

Ashby, M.F., 1970. Deformation of plastically non-homogeneous materials. Philos. Mag. 21, 399–424.

Bassani, J.L., 2001. Incompatibility and a simple gradient theory of plasticity. J. Mech. Phys. Solids 49, 1983–1996.

Cheng, Z., Zhou, H., Lu, Q., Gao, H., Lu, L., 2018. Extra strengthening and work hardening in gradient nanotwinned metals. Science 362, eaau1925.

Fang, T.H., Li, W.L., Tao, N.R., Lu, K., 2011. Revealing extraordinary intrinsic tensile plasticity in gradient nano-grained copper. Science 331, 1587–1590.

Fleck, N.A., Muller, G.M., Ashby, M.F., Hutchinson, J.W., 1994. Strain graident plasticity–theory and experiment. Acta Metall. Mater. 42, 475–487.

Gudmundson, P., 2004. A unified treatment of strain gradient plasticity. J. Mech. Phys. Solids 52, 1379–1406.

Lele, S.P., Anand, L., 2008. A small-deformation strain-gradient theory for isotropic viscoplastic materials. Philos. Mag. 88, 3655–3689.

Lele, S.P., Anand, L., 2009. A large-deformation strain-gradient theory for isotropic viscoplastic materials. Int. J. Plasticity 25, 420–453.

Li, J., Soh, A.K., 2012. Modeling of the plastic deformation of nanostructured materials with grain size gradient. Int. J. Plasticity 39, 88–102.

Li, J., Weng, G.J., Chen, S., Wu, X., 2017. On strain hardening mechanism in gradient nanostructures. Int. J. Plasticity 88, 89–107.

Lu, K., 2016. Stabilizing nanostructures in metals using grain and twin boundary architectures. Nat. Rev. Mater. 1, 16019.

Ma, E., Zhu, T., 2017. Towards strength–ductility synergy through the design of heterogeneous nanostructures in metals. Materials Today 20, 323–331.

Mughrabi, H., 2006. Deformation-induced long-range internal stresses and lattice plane misorientations and the role of geometrically necessary dislocations. Philos. Mag. 86, 4037–4054.

Niordson, C.F., Hutchinson, J.W., 2003. On lower order strain gradient plasticity theories. Eur. J. Mech.–A/Solids 22, 771–778.

Nix, W.D., Gao, H.J., 1998. Indentation size effects in crystalline materials: a law for strain gradient plasticity. J. Mech. Phys. Solids 46, 411–425.

Wei, Y., Li, Y., Zhu, L., Liu, Y., Lei, X., Wang, G., Wu, Y., Mi, Z., Liu, J., Wang, H., Gao, H., 2014. Evading the strength-ductility trade-off dilemma in steel through gradient hierarchical nanotwins. Nat. Commun. 5, 3580.

Wu, X., Jiang, P., Chen, L., Yuan, F., Zhu, Y.T., 2014. Extraordinary strain hardening by gradient structure. Proc. Natl. Acad. Sci. U.S.A. 111, 7197–7201.

Wu, X., Zhu, Y., 2017. Heterogeneous materials: a new class of materials with unprecedented mechanical properties. Mater. Res. Lett. 5, 527–532.

Zeng, Z., Li, X., Xu, D., Lu, L., Gao, H., Zhu, T., 2016. Gradient plasticity in graident nano-grained metals. Extrem. Mech. Lett. 8, 213–219.